Additive Manufacturing 48 (2021) 102424

Contents lists available at ScienceDirect

Additive Manufacturing

journal homepage: www.elsevier.com/locate/addma

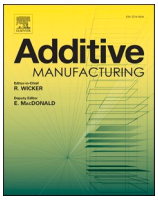

Research paper

A bead sequence-driven deposition pattern evaluation criterion for lowering residual stresses in additive manufacturing

Li Sun [a], Xiaobo Ren [b], Jianying He [a], Zhiliang Zhang [a,*]

[a] Department of Structural Engineering, Norwegian University of Science and Technology (NTNU), Trondheim 7491, Norway
[b] Department of Materials and Nanotechnology, SINTEF Industry, Trondheim 7456, Norway

ARTICLE INFO

Keywords:
Additive manufacturing (AM)
Deposition pattern
Temperature fields
Residual stress
Bead sequence-driven
Real-time optimization

ABSTRACT

Deposition patterns can significantly influence the distribution and magnitude of residual stress in additively manufactured parts. Time-consuming thermal-mechanical simulations and costly experimental studies are often required to identify the optimal patterns. A simple and generic method to evaluate and optimize the deposition pattern for the purpose of minimizing residual stress is in urgent need. To overcome the shortcomings of the current practice, here we propose a novel pattern evaluation criterion. Starting from the discretization of the deposition pattern by a series of sequence numbers, we introduce two interconnected concepts. The first is called "equivalent bead sequence number" which can be physically interpreted as an index of the localized heat accumulation induced by the deposition process. Based on this point-wise "equivalent bead sequence number", the second concept called "bead sequence number dispersion index" which can be considered as a representation of the global heat accumulation gradient, is proposed as a criterion for assessing the resulting residual stress. The temperature fields and residual stresses of a square part with six typical deposition patterns predicted by thermo-mechanical finite element simulations are used to develop and verify the proposed criterion. It is found that the "equivalent bead sequence number" of a given pattern is closely correlated to the distribution of the associated temperature and residual stress. More interestingly, both the highest equivalent and highest maximum principal residual stress of a pattern linearly increase with its corresponding value of "bead sequence number dispersion index". Guided by this relation, two new patterns with lower residual stress are developed and evaluated. Among all the patterns considered, the so-called S pattern shows the lowest value of the "bead sequence number dispersion index" which corresponds to the lowest residual stress. The proposed sequence-driven approach provides a new candidate for real-time evaluation and optimization of the deposition pattern in additive manufacturing.

1. Introduction

Residual stress is inherent in an additive manufacturing process due to high temperature gradient [1]. Residual stress can impact a wide range of properties and performances of printed components, i.e., fatigue life, corrosion resistance, crack propagation behavior, porosity, distortions, etc. [2–4]. Since a deposition pattern dictates the transient temperature distribution [5,6], it has a remarkable effect on residual stress distribution. In order to minimize the effect of residual stress and improve part quality, considerable efforts have been devoted to optimizing the deposition patterns.

The residual stress in additively manufactured components has two origins: residual stress generated during the manufacturing process and residual stress redistributed by removing the constraints. For a given component, the former is mainly determined by the local temperature gradient caused by the traveling heat source [2]. A more uniform local temperature gradient will produce lower residual stress. When removing the constraints, some stresses will be released and thus the final residual stress will be redistributed. The amount of the released stress is proportional to the uniformity of global heat accumulation [7]. In general, both local temperature gradient and global heat accumulation gradient are important for residual stress and strongly correlated with deposition patterns. At present, five representative deposition patterns are commonly used in AM: raster, Zigzag, in-out spiral, out-in spiral, and fractal [8]. Based on these basic patterns, several combined deposition patterns have been proposed in the literature to reduce the residual

* Corresponding author.
E-mail address: zhiliang.zhang@ntnu.no (Z. Zhang).

https://doi.org/10.1016/j.addma.2021.102424
Received 12 May 2021; Received in revised form 27 September 2021; Accepted 21 October 2021
Available online 29 October 2021

stress in printed parts, such as alternate-line pattern, island pattern [9], multi-laser scanning pattern [10], and intermittent pattern [11]. A large amount of numerical and experimental studies has been performed to compare these patterns in terms of residual stress and the ranking of these patterns varies with the structures and the processes [12–17]. Despite the complexity of the deposition patterns, we can generalize that there are mainly four factors affecting the distribution of residual stress: deposition or scan vector length, distance between two successive deposition vectors, deposition direction, and deposition orientation of each layer.

The deposition or scan vector length is a vital factor affecting residual stress [18]. Kruth et al. [14,19] experimentally investigated the effect of vector length on the residual stress under different patterns and revealed that longer scan vectors caused higher residual stress along the direction of the scan vector. Parry et al. [20] concluded that longitudinal stress (parallel to the scan vector) increased with the scan vector length because of the larger thermal gradient parallel to the scan vector. Schröffer et al. [9] proposed an island pattern and reported that the shortened vector length helped to reduce residual stress. Lu et al. [13] studied the effect of island size on residual stress in a selective laser melting and found that island with a dimension of $5\text{mm} * 5\text{mm}$ exhibited lower residual stress than the islands with a dimension of $7\text{mm} * 7\text{mm}$ and $3\text{mm} * 3\text{mm}$. Interestingly, the numeral results by Parry et al. showed that the laser scan pattern became less important for the scan vector length beyond 3 mm [21].

The distance between two successive deposition vectors is another important factor that can significantly affect heat transfer and temperature distribution. It is well agreed that residual stress is related to the degree of heat accumulation which can be regulated by the deposition vector sequence [7,11,22]. Hence, another general optimization strategy for reducing residual stress is to avoid the subsequent pass adjacent to the previous one. Based on this finding, the alternate-line pattern which resulted in lower residual stress than raster and Zigzag patterns was proposed [17]. Zaeh et al. [22] compared the use of the island, unidirectional, and alternating scanning patterns, and found that the island pattern yielded the lowest level of residual stress while the alternating showed an intermediate level of stress between the two unidirectional patterns. Combining the studies of the aforementioned scan vector length and the distance between the vectors, an intermittent strategy would be to divide a geometry into small islands and to further reduce the heat accumulation by controlling the scanning order. Ramos et al.[11] proposed this strategy for a selective laser melting process and the numerical study revealed a significant reduction in residual stress.

Deposition direction will also influence the residual stress. For example, for the out-in spiral pattern, heat is accumulated inward and concentrated in the center part. In contrast, heat is dissipated outward under the in-out spiral pattern and thus temperature distribution becomes more homogeneous. Consequently, the out-in spiral pattern results in higher residual stress than the in-out pattern [15,23]. Sun et al. [7] proposed a so-called S pattern that possesses multiple advantages, i.e. adjustable pass length, fewer adjacent deposition segments, and alternative directions. In numerical and experimental studies, it was shown that the S pattern generates lower residual stress, less porosity, and smaller grain than other patterns [24].

For multilayer structures, rotating the deposition orientation can generate a more uniform residual stress distribution. Bartlett et al. [25] studied the residual stress development process via used digital image correlation method. It was found that the residual stress on the top surface is determined by local scanning orientation and also interactions between layers. The sequential re-heating and cooling of the new surface result in the residual stress distribution changing dynamically between layers and become more heterogeneous. Kruth et al. [14] performed an experimental study and observed that residual stress could be reduced if the initial hatch angle for each layer is changed. Cheng et al. [23] evaluated the residual stresses of the patterns with different hatch angles (0°, 45°, 67°, 90°), and the results show that the scanning pattern with hatch angle 45° yields the lowest residual stress.

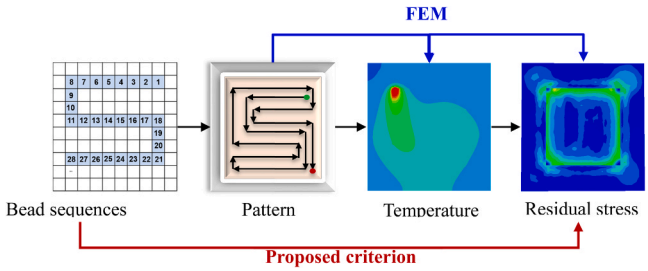

Fig. 1. Illustration of the FEM based and the proposed evaluation criterion. For the FEM-based, expensive thermal-mechanical analyses of the entire part over the complete process period are required. In the proposed criterion, the single deposition bead is regarded as a basic element and the pattern is represented by the bead sequence. A direct relationship between the bead sequence and the final residual stress is sought.

Although a large number of studies have compared the patterns and analyzed the affecting factors, a pattern evaluation and optimization criterion combining these factors is missing. It also should be noted that in all these studies, full-scale finite element models or experimental studies were used to evaluate the residual stress under different deposition patterns. One main challenge for the numerical method is the exponentially increasing computational cost required to simulate the deposition processes for large area 2D and multi-layered 3D parts. Although some fast solution methods for computing transient temperature fields have been proposed [26–29], rapid and effective assessment of residual stress of AM parts remains a challenge. A simple but general method to evaluate residual stress under an arbitrary pattern and optimize deposition strategies for different structures is highly desired.

WAAM technology is a promising technology for fabricating large metal components with high deposition rates for a variety of metallic alloys. However, the residual stress remains a challenge for the final product of the WAAM process. Usually, the G-code translated from CAD models is utilized to control the automated machine tools to deposit materials point by point, layer by layer [27]. In this work, a G-code informed evaluation criterion for lowering residual stresses in WAAM is proposed. We envisage that a deposition pattern is composed of a series of bead sequence numbers. By linking the discrete sequence number to the localized heat accumulation and the global heat accumulation gradient of a printed part, we propose a sequence-driven criterion for evaluating the deposition patterns. The definition and calculation method are introduced in Section 2. Thermal-mechanical finite element simulations are performed to provide data for developing and verifying the proposed criterion. The modeling procedure and simulation results are presented in Section 3. In Section 4, the relationship between the proposed evaluation criterion and residual stress is discussed. Two new deposition patterns guided by the proposed criterion are explored. The conclusions are summarized in Section 5.

2. Deposition pattern evaluation criterion

2.1. G-code informed evaluation criterion

Thermal-mechanical finite element method (FEM) simulations are widely used to evaluate the effect of different deposition patterns on the magnitude of residual stress. As illustrated in Fig. 1, the FEM simulation usually includes two steps: firstly, a thermal analysis is carried out to predict the temperature field for a predefined deposition pattern; then, the residual stress is obtained from a mechanical analysis with the temperature field as the input. However, the thermal-mechanical simulation is so computationally demanding that it cannot be directly applied to the optimization of the patterns.

In the present study, in order to avoid the time-consuming FEM simulations, a novel method to establish the relationship between the

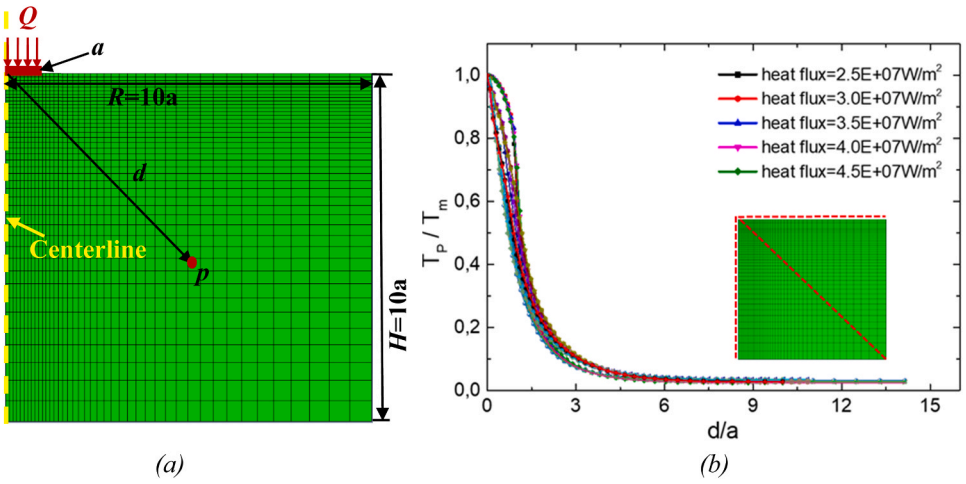

Fig. 2. Finite element model and the temperature distributions (a) the axisymmetric point heat source model (heat source radius a, model radius =10a, height H=10a). Axisymmetric boundary condition is applied in the centerline, shown by the yellow dash line.The heat source is located at the center of the top surface; (b) normalized nodal peak temperature versus normalized distance from the nodes to the heat source center point. The peak temperature T_p(Unit: ℃) that the nodes along the horizontal, vertical, and diagonal directions, as illustrated by the red dotted lines, have experienced in the deposition process is normalized by the maximum temperature the whole model experienced Tm(Unit: ℃).The distance from the nodes to the heat center d is normalized by the heat source radius a. (For interpretation of the references to colour in this figure, the reader is referred to the web version of this article.)

pattern and residual stress is proposed. As known, in WAAM, the melted beads were deposited one by one and layer by layer to create three-dimensional objects [30–32]. Since different deposition patterns will lead to the different generation time and ordering of the beads, a deposition pattern can be represented by a series of bead sequence numbers, as shown in Fig. 1. Hence, the underlying feature determining the residual stress is the bead sequence number which can be directly obtained from the AM G-Code design. The aim of this work is to develop an explicit relationship between the bead sequence number and the residual stress.

It is known that the extent of heat accumulation as a result of the processing and deposition pattern determines the residual stress distribution and distortion [33]. In general, the residual stress and distortion escalate with the increase of the degree of heat concentration. Based on this observation, Ren et al. [34] proposed a method to identify the optimal pattern with low distortion. In this method, an evaluation criterion including two steps was proposed to evaluate the extent of localized heat accumulation and the uniformity of global heat accumulation gradient, respectively. The first step is to evaluate the average and maximum temperatures within the moving molten pool region, and the second step is to calculate the temperature distribution variance of the whole part. The results based on this evaluation criterion agree well with the experimental results. However, the criterion is proposed for the pattern evaluation with respect to distortion, and residual stress is not studied. In addition, the evaluation procedure is based on the real temperature distributions and time-consuming FEM simulations are required. Consequently, this evaluation procedure cannot be used to screen the deposition patterns in real-time based on the AM G-Code design or as a guideline to develop new patterns for lowering residual stress.

As mentioned before, the final distortion and the uniformity of residual stress distribution are determined by the degree of heat concentration and positively correlated with each other. In this work, we will attempt to design two G-Code-informed indexes, to represent the localized heat concentration and global heat accumulation gradient, respectively. With the aim of reducing residual stress, the beads around a given position should be deposited as staggered as possible over a time scale in order to suppress the localized heat accumulation. The printed beads at any time should be distributed as evenly as possible over the space with the purpose to reduce the global heat accumulation gradient. In order to evaluate the beads dispersion in time and space scales, bead sequence number and bead coordinates will be introduced. The indexes of the localized heat concentration and global heat accumulation gradient of a printed part will be computed based on the discrete bead sequence number, and a deposition pattern evaluation procedure will be developed based on the indexes.

2.2. Evaluation criterion development

In this section, the heat influence zone (HIZ) will be introduced to evaluate the degree of localized heat accumulation, and the method for calculating the size of HIZ will be presented first. Then the concept of "equivalent bead sequence number" will be proposed and physically interpreted as an index of the localized heat accumulation generated by the deposition process. Based on this point-wise "equivalent bead sequence number", the second concept called "bead sequence number dispersion index" which can be considered as a representation of the global heat accumulation gradient is discussed in detail. It will be used as a criterion for assessing residual stress.

2.2.1. Heat influence zone (HIZ)

We start by discretizing the deposition area into square beads. The localized heat accumulation at a discretized bead is affected by the deposition sequence of the surrounding beads within a certain distance. In order to evaluate the localized heat accumulation of each bead, we utilize the concept of HIZ defined by Roy et. al [29]. HIZ is the maximum distance from the heat source, and any heated deposition within this distance will have a significant thermal effect. In Ref. [29], the size of HIZ was obtained by leveraging an analytical solution to the transient heat equation with a point heat source on a semi-infinite body. The material used was polymer, and the HIZ size was calculated by setting a temperature limit of 10% of the glass temperature (Unit: ℃).

The material considered in this study is aluminum alloy AA2319. In order to study the HIZ, an axisymmetric single point heat source model was analyzed using ABAQUS, as shown in Fig. 2, analogous to the previous work [35]. Mesh sensitivity analysis has been performed. Both thermal convection and radiation heat loss are considered. During the heating process, five sets of surface heat flux (Q) ranging from $2.5 * 10^7 W/m^2$ to $4.5 * 10^7 W/m^2$ are applied to the center area of the cylindrical model through a circular plane (see Fig. 2(a)). The heating stage lasts for 1 s, consistent with the deposition process with a speed of 10 mm/s. In the subsequent cooling stage, the material will cool down to

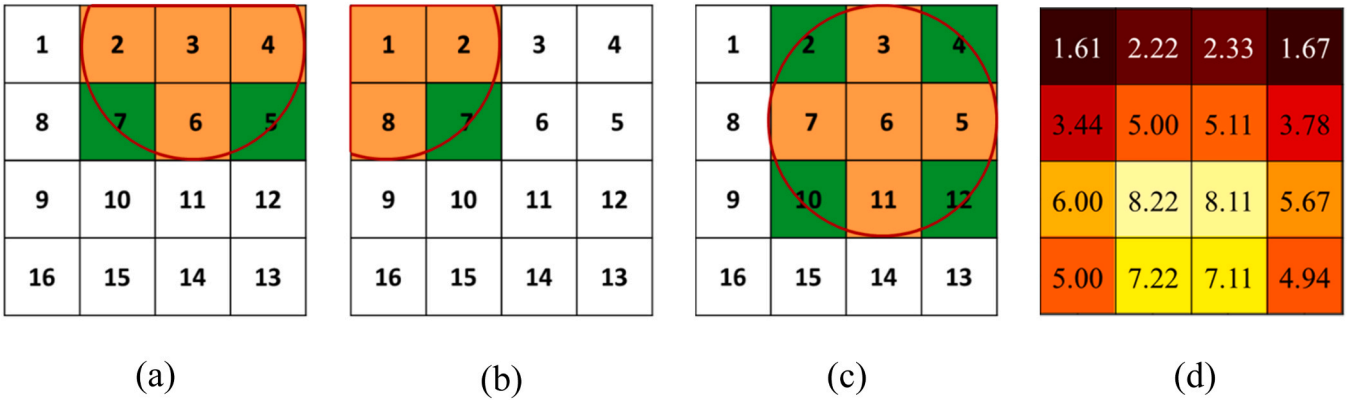

Fig. 3. Different types of beads and $\overline{N}$ distribution. (a) middle bead (number 6) with 8 adjacent beads (b) corner bead (number 1) with 3 adjacent beads; (c) side bead (number 3) with 5 adjacent beads; (4) $\overline{N}$ distribution.

the ambient temperature naturally. The nodal peak temperature (T_p) normalized by the maximum temperature the whole model experienced (T_m) as a function of normalized distance (d/a) is plotted in Fig. 2(b). d is the distance from the nodes to the heat source and a is the radius of the heat source.

It can be observed that the temperature distribution becomes flat when the normalized peak temperature is less than 0.1. Similar to the threshold defined by Roy et. Al [29], a limit of 10% T_m is set in this study. Fig. 2 clearly shows that the condition $T_{p/}\ T_m = 0.1$ corresponds to $d/a \sim 3$. The size of the HIZ used in this study is therefore taken as three times the radius of the heat source.

2.2.2. Equivalent bead sequence number ($\overline{N}$)

Because the deposition area is now divided into equal-sized beads, the beads can be numbered according to the generation time which is determined by the planned deposition pattern. We take the Zigzag pattern as an example to show the numbering rule. The number of each bead represents the sequence of each bead. It can be seen in Fig. 3 that the bead is deposited from the left to the right on the top row (from 1 to 4). For a second row, the beads move in the opposite direction (from 5 to 8). Then a turn back is repeated for the third row (from 9 to 12).

As stated in Section 2.2.1, the HIZ is defined as the area within three

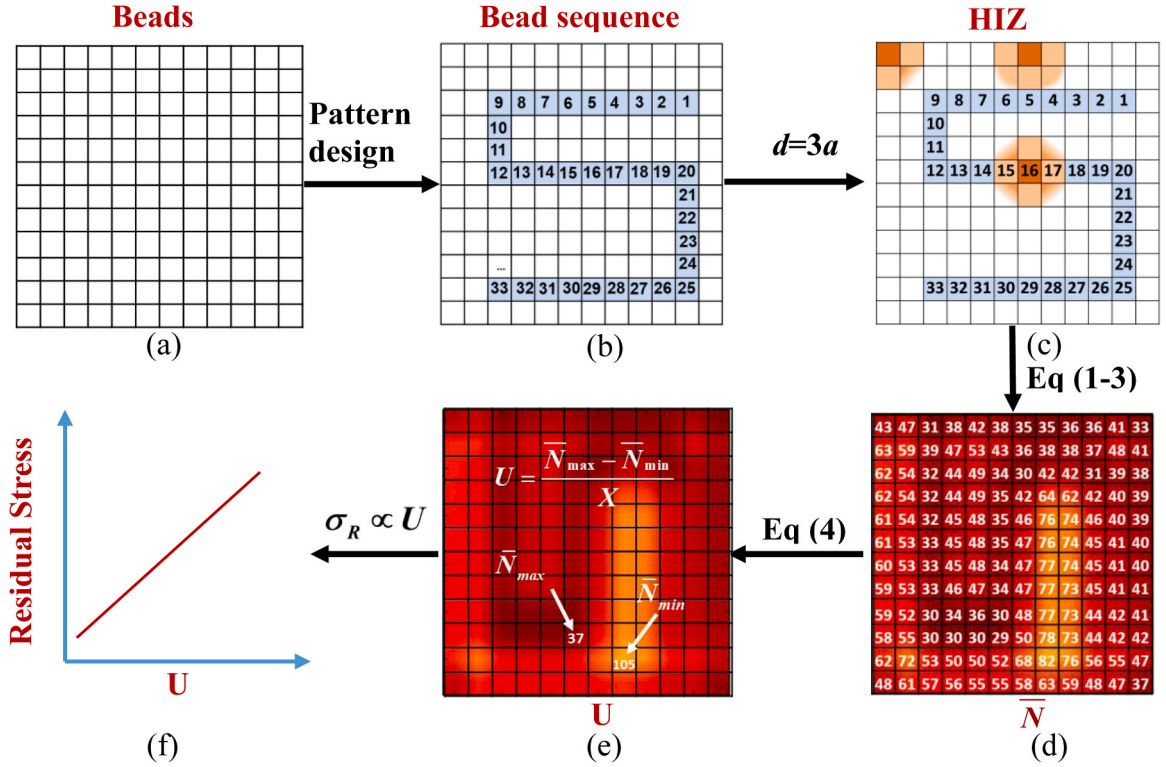

Fig. 4. Deposition pattern evaluation procedure.(a) The deposition area is discretized into square beads. (b) All beads are numbered according to the printing sequence. (c) The size of HIZ varying with the type of beads isdetermined by the single point heat source model. (d) Based on the type and the HIZ, the of each bead will be calculated by Eqs. (1–3). (e) The U will be calculated by Eq. (4). (f) The established relationship between residual stress and the U will be applied to evaluate the deposition pattern with regard to the residual stress level.

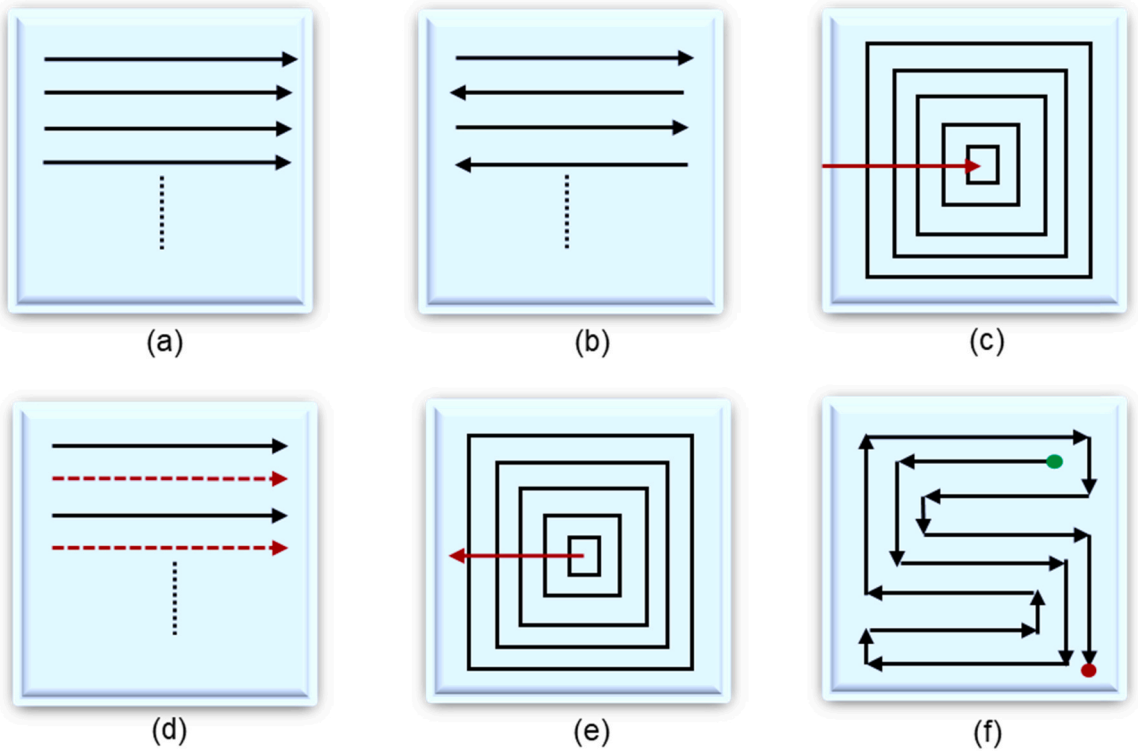

Fig. 5. The deposition patterns considered in this study: (a) Raster; (b) Zigzag; (c) Out-in spiral; (d) Alternate-line; (e) In-out spiral; (f) S (the green and red dots are the starting and ending points, respectively) [7].

times the radius of the heat source. For an AM deposition process, half of the bead width can be regarded as the radius of the heat source. Accordingly, the HIZ (denoted as the red curve) includes almost the entire adjacent beads and the deposited bead (marked in orange), as well as about nearly half of the diagonal beads (marked in green), as indicated in Fig. 3.

In order to make the proposed criterion applicable for different processes and facilitate its practical application, the assessment of localized heat accumulation has been simplified. The heat influence zone is regarded as a local calculation unit. A concept called "equivalent bead sequence number ($\overline{N}$)" is proposed, referring to the average value of the bead sequence number of the beads in the HIZ.

Depending on the geometric position, the beads can be classified into three types: middle beads (number 7, 6, 10, and 11), corner beads (number 1, 4, 16, and 13), and side beads (number 2, 3, 5, 8, 9, 12, 14 and 15). It can be easily seen that different types of beads will have different numbers of girds in the HIZ. For the middle beads, e.g. number 6, the HIZ includes 9 beads, see Fig. 3(a), while for the side beads and the corner beads, e.g. numbers 1 and 3, there are 4 and 6 beads in the HIZ as shown in Fig. 3(b) and (c), respectively. By assigning appropriate weight to each type of bead, we obtain the following equations for calculating the $\overline{N}$ for a bead with coordinate (i, j) (i is the row number and j is the column number)

$$\text{Middle}: \overline{N}_{i,j} = \left[\left(n_{i-1,j-1}+n_{i-1,j+1}+n_{i+1,j-1}+n_{i+1,j+1}\right)/2+\left(n_{i-1,j}+n_{i,j}+n_{i+1,j}+n_{i,j-1}+n_{i,j+1}\right)\right]/9 \quad (1)$$

$$\text{Corner}: \overline{N}_{i,j} = \left(n_{i+1,j+1}/2+n_{i,j}+n_{i+1,j}+n_{i,j+1}\right)/9 \quad (2)$$

$$\text{Side}: \overline{N}_{i,j} = \left[\left(n_{i+1,j-1}+n_{i+1,j+1}\right)/2+\left(n_{i,j}+n_{i+1,j}+n_{i,j+1}+n_{i,j-1}\right)\right]/9 \quad (3)$$

where $n_{i,j}$ is the original deposition sequence number of the bead in the i row and j column redefined by the deposition patterns. It should be noted that only half of the heat contribution of the diagonal bead is accounted in the above equations and $\overline{N}$ is calculated as the sum of the bead sequence numbers in the HIZ divided by nine. Hence, Eqs. (1–3) is associated with two aspects: the area of HIZ and the average bead sequence number in HIZ.

The $\overline{N}$ value indicates the localized heat accumulation in spatial and time scales. In the spatial scale, the localized heat accumulation consists of the heat contributions from inside and outside HIZ: (1) since the heat input is considered the same for each bead, the area of the HIZ is used to represent the heat contribution from inside the HIZ; (2) the equivalent bead sequence number depends on the average value of the bead

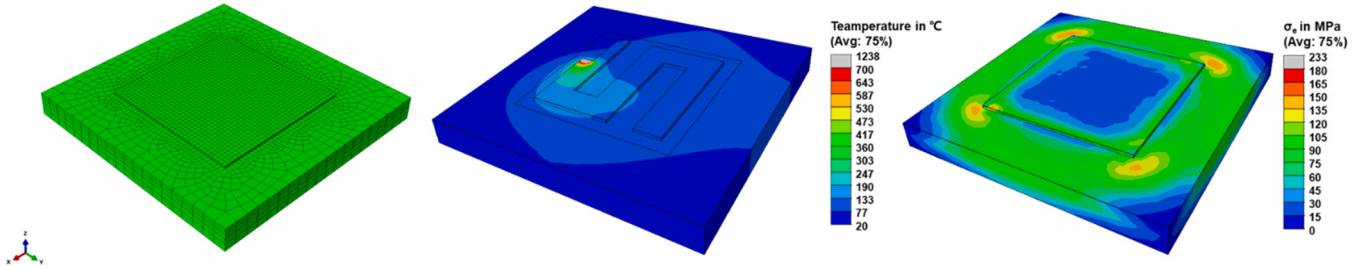

Fig. 6. The finite element model, (a) mesh; (b) thermal simulation; (c) mechanical simulation.

sequence number which represents the average printing order. As we know, the heat accumulation of a given location increases with the printing process. Therefore, the average printing order is related to the heat contribution from the outside of the HIZ. More importantly, the uniformity of $\overline{N}$ represents the extent to which deposition beads are staggered with time, which is positively related to the degree of heat accumulation on the time scale. Considering all the physical interpretations, $\overline{N}$ is proposed as an index of localized heat accumulation.

Based on Eqs. (1–3), the $\overline{N}$ values of the beads in the example zigzag deposition pattern are calculated and displayed in Fig. 3(d). The color system has been assigned in the following manner: the larger the $\overline{N}$ value is, the darker the color of the corresponding grid is. The distribution of the point-wise $\overline{N}$ represents the degree of the bead sequence number dispersion in time and space scale which correlates to the uniformity of global heat distribution.

2.2.3. Bead sequence number dispersion index (U)

Based on the point-wise $\overline{N}$, a second concept called "bead sequence number dispersion index (U)" is proposed. The U is defined as the normalized range of $\overline{N}$, as shown in Eq. (4).

$$U = \frac{Max\left(\overline{N}_{i,j}\right) - Min\left(\overline{N}_{i,j}\right)}{X} \tag{4}$$

Where X is the total number of the discrete beads. Since the deposition process is assumed to be continuous, the $\overline{N}$ will also be continuous. Thus, the U can be considered as a direct representation of the global heat accumulation gradient. A larger U indicates a higher global heat accumulation gradient, more heterogeneous temperature distribution and higher residual stress. A simple criterion for assessing the residual stress (σ_R) is therefore proposed,

$$\sigma_R \propto U \tag{5}$$

This simple criterion will be validated by comparing with the FEM results in the next section. If it is true, the proposed criterion is of great significance since the U can be directly computed from the G-Code without the need of performing time-consuming finite element analyses. The proposed deposition pattern evaluation procedure is presented in Fig. 4. The U will be firstly calculated from a pre-defined pattern, then solely based on the U, we can immediately compare the deposition patterns and evaluate the resulting residual stress level.

3. Verification of the proposed evaluation criterion

3.1. Numerical modeling procedure

In order to verify the proposed criterion, the temperature field and residual stresses of a square part with six typical deposition patterns are predicted by thermo-mechanical finite element simulations. A previously created sequential thermal-mechanical model [7] is used in this study, as shown in Fig. 6. The geometries of the deposition layer and substrate are $120\text{mm} * 120\text{mm} * 2.23\text{mm}$ and $200\text{mm} * 200\text{mm} * 20\text{mm}$, respectively. A WAAM process is studied by ABAQUS. The material is aluminum alloy AA2319. The pass width and layer thickness are 10 mm and 2.23 mm, respectively. The deposition speed is 10 mm/s. The total deposition time is 144 s and then the model cools down to room temperature naturally. The entire simulation process includes thermal analysis and mechanical analysis. In the thermal analysis, the temperature field is studied as shown in Fig. 6(b). Then, the temperature field is applied to the mechanical model (Fig. 6(c)) to calculate residual stress.

Table 1
Heat source related parameters used in the finite element analyses.

Parameters	b	c	Q	a_f	a_r	f_f	f_r
Values	5 mm	2.3 mm	5000 W	2 mm	4 mm	0.6	1.4

In the numerical simulation, six patterns shown in Fig. 5 are studied. The deposition patterns are defined as a set of data in the AM module of ABAQUS software. This set of data includes all the necessary information about the deposition pattern including the deposition time, the spatial location of the deposited material, and bead cross-section area. The elements and materials properties are activated at the appropriate time according to the set of data. To make the simulation results of different patterns comparable, all the simulations are performed under the same process parameters and the deposition pattern is the only variable.

3.1.1. Thermal analysis

In thermal simulations, the governing equation for the heat transfer process is formulated by using the energy equation:

$$\rho C_P(T)\frac{dT}{dt} + \rho\frac{d(fL)}{dt} = Q\left(r,t\right) - \nabla q(r,t) \tag{6}$$

where ρ is density, C_p is specific heat, T is temperature, t is time, L is the latent heat of fusion, r is relative reference coordinate, Q is the energy density of heat source, and f is the liquid fraction, which is used to calculate the latent heat during the deposition process. It's one when the temperature is greater than the liquidus temperature, and zero when the temperature is less than the solidus temperature and varies linearly between zero and one when the temperature is between the liquidus temperature and the solidus temperature. ∇q is heat loss from surface convection and radiation.

The element type used in the FE model is 8-node linear heat transfer brick (DC3D8). Both ambient temperature and the initial temperature of the substrate are 20 °C. The conduction loss of the bottom surface is modeled by an equivalent conductivity coefficient (123 W/m^{2}k) [36], while the other surfaces of the model are subjected to radiation (0.8) and convection heat loss (8.5 W/(m^{2}K). After deposition, the model naturally cools down to room temperature in 3000 s.

A double-ellipsoid heat source model is applied to the single deposition layer, which can be described as: [37]:

$$Q_{f/r}(x,y,z) = \frac{6\sqrt{3}Q * f_{f/r}}{a_{f/r} * b * c * \pi\sqrt{\pi}} \exp\left(-\frac{3x^2}{a_{f/r}^2} - \frac{3y^2}{b^2} - \frac{3z^2}{c^2}\right) \tag{7}$$

Table 2
Physical properties of aluminum alloy AA2319 [38,39].

Parameters	Mass density	Liquidus temperature	Solidus temperature	Initial temperature	Latent heat
Values	2823 kg/m^3	643 ℃	543 ℃	20 ℃	370,000 J/kg
Temperature (℃)	Conductivity (W/m℃)	Specific heat (J/Kg℃)	Thermal expansion coefficient (×10E-5/℃)	Young's modulus (GPa)	Yield stress (MPa)
20	123	832	2.12	72.5	243
50	129	862	2.18	71.6	230
100	140	910	2.24	70.1	207
150	149	938	2.3	66.7	187
200	155	952	2.36	63.1	166
250	158	962	2.42	59	145
300	155	969	2.47	55	123
350	150	1030	2.47	46.1	72
400	144	1060	2.47	36.7	35
450	144	1060	2.47	26.7	25
500	144	1060	2.47	16.8	15
550	144	1060	2.47	8.14	6
600	203	1060	2.47	0.23	5
650	252	1060	2.47		

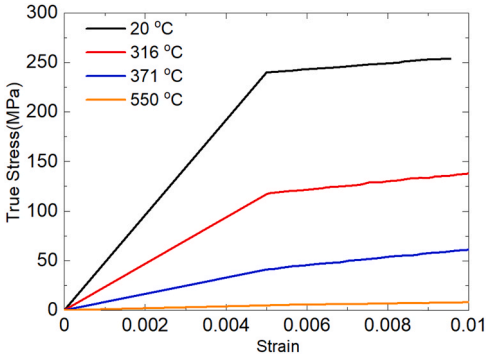

Fig. 7. Stress-strain property of aluminum alloy AA2319 [38,39].

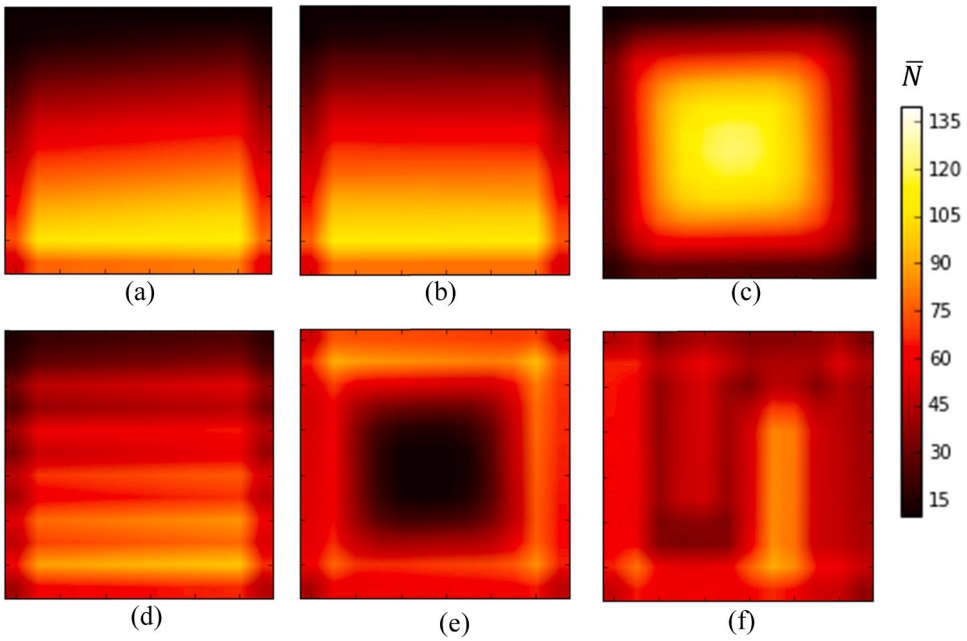

Fig. 8. The $\overline{N}$ distribution of the six patterns (a) Raster; (b) Zigzag; (c) Out-in spiral; (d) Alternate-line; (e) In-out spiral; (f) S.

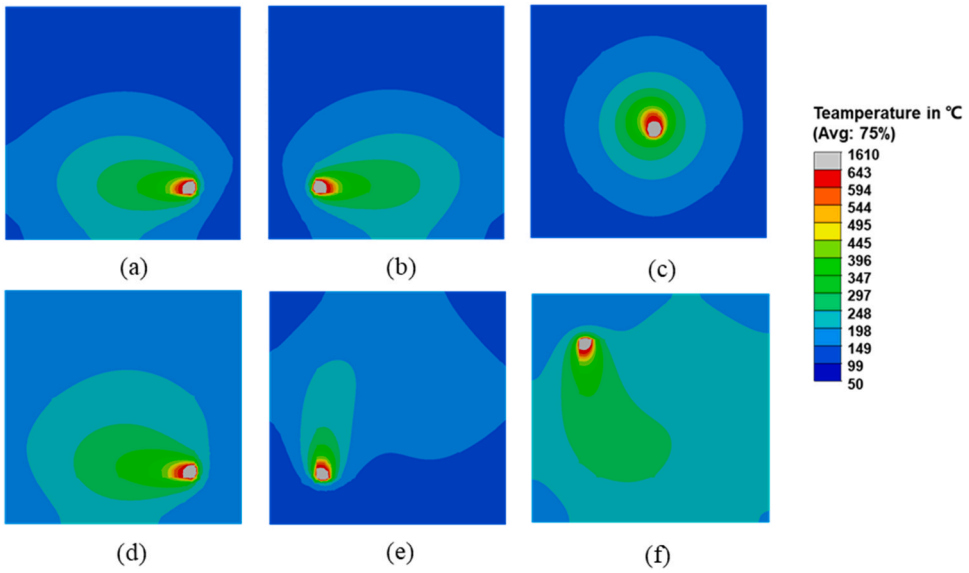

Fig. 9. The transient temperature fields of the six patterns at the end of the deposition process, (a) Raster; (b) Zigzag; (c) Out-in spiral; (d) Alternate-line; (e) In-out spiral; (f) S. The grey color shows the melting zone.

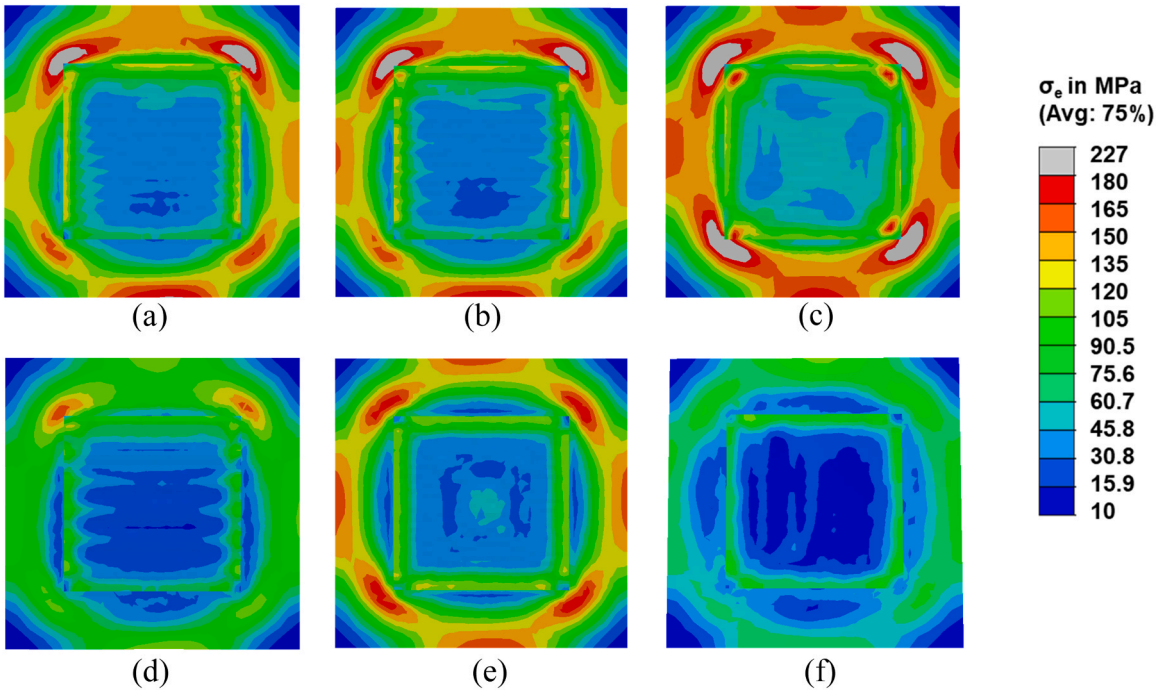

Fig. 10. Equivalent residual stress fields of the six typical deposition patterns, (a) Raster; (b) Zigzag; (c) Out-in spiral; (d) Alternate-line; (e) In-out spiral; (f) S.

where a_f and a_r are the length of the front and rear ellipsoid of the heat source, c and b are the depth and half-width of the heat source, Q is the power input, f_f and f_r are the fraction factors of the heat flux in the front and rear parts, respectively. The values of the parameters used in this work are shown in Table 1. The paths of heat source, which are the same as the paths of adding material, are defined in the AM module. The heat source moves along with the path of adding elements during the simulation process. The temperature-dependent material properties of used material aluminum alloy AA2319, i.e. the thermal conductivity coefficient, specific heat, thermal expansion coefficient, temperature-dependent yield stress, and Young's modulus, same as those of the point heat source model in section 2.3.1, are obtained from Ref. [38,39] and listed in Table (2). All material properties are considered to be isotropic and homogenous.

3.1.2. *Mechanical analysis*

After the thermal analysis, the resulting transient temperature field is coupled to the subsequent mechanical analysis to calculate residual stress. In the mechanical simulation process, the same finite element mesh as the thermal model is used, and the same material addition process is performed, while the element type is changed to 8-node brick element with reduced integration (C3D8R). The bottom of the substrate is fixed during the deposition process, and the constraint is removed after the material naturally cools down to room temperature. The theory of thermal-mechanical analysis can be found in [40]. The temperature-inducing softening of the stress-strain curves is considered.

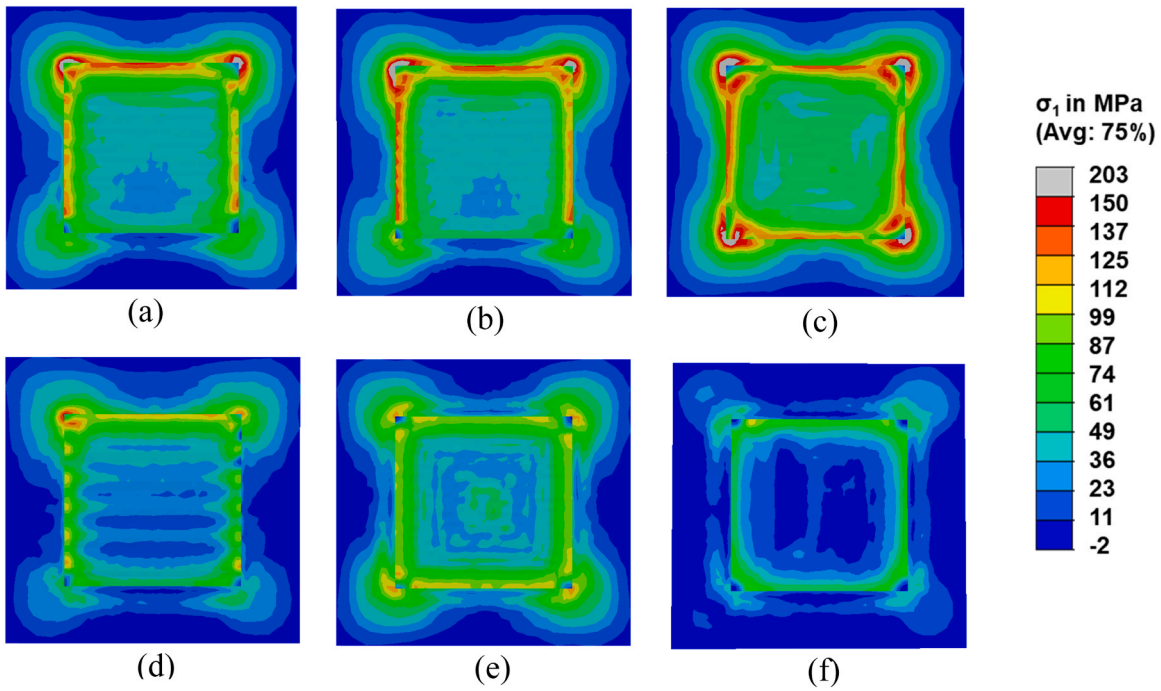

Fig. 11. Maximum principal residual stress fields of the six deposition patterns, (a) Raster; (b) Zigzag; (c) Out-in spiral; (d) Alternate-line; (e) In-out spiral; (f) S.

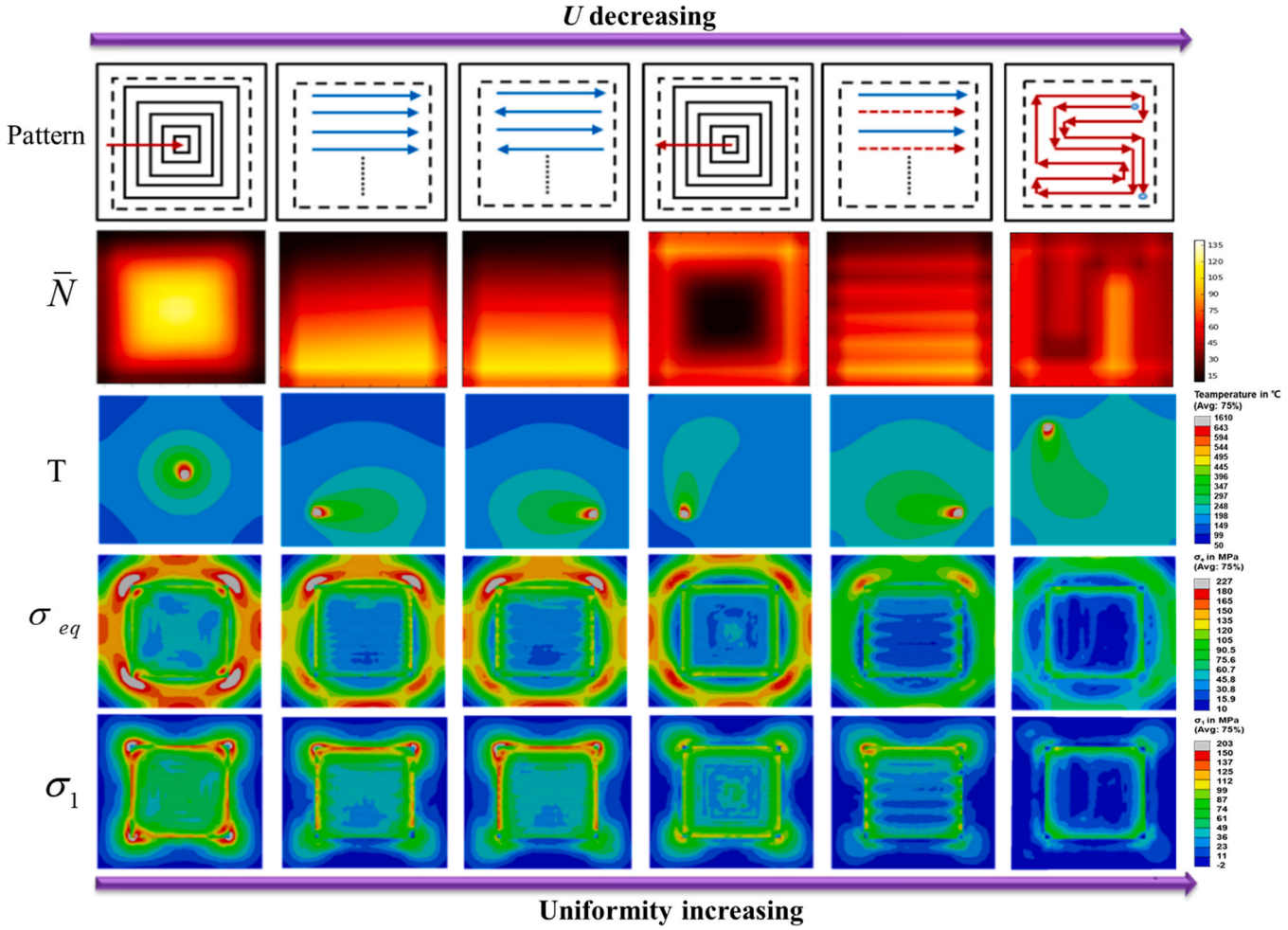

Fig. 12. Summary of the patterns, $\overline{N}$ distributions, temperature distributions, and residual stresses distributions (σ_e and σ_1). The patterns are arranged in the order of decreasing U. The $\overline{N}$ distribution, temperature distribution, and residual stresses distribution become more uniform as the U decrease.

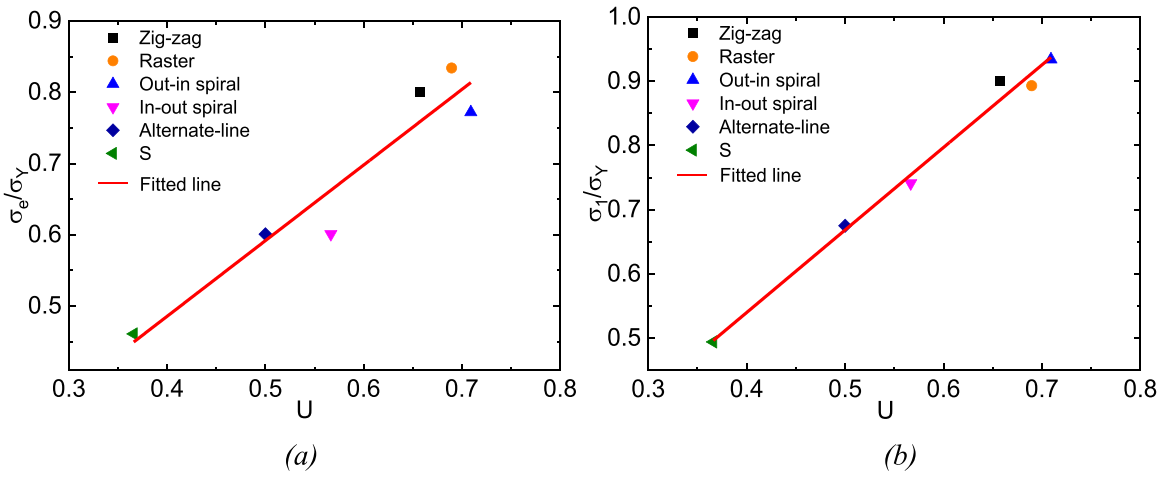

Fig. 13. Normalized residual stresses versus U: (a) σ_e; (b) σ_1. The U of different patterns are calculated by Eq. (4). σ_e and σ_1 are normalized by yield stress (σ_Y=243 MPa) of aluminum alloy AA2319 at 20 ℃.

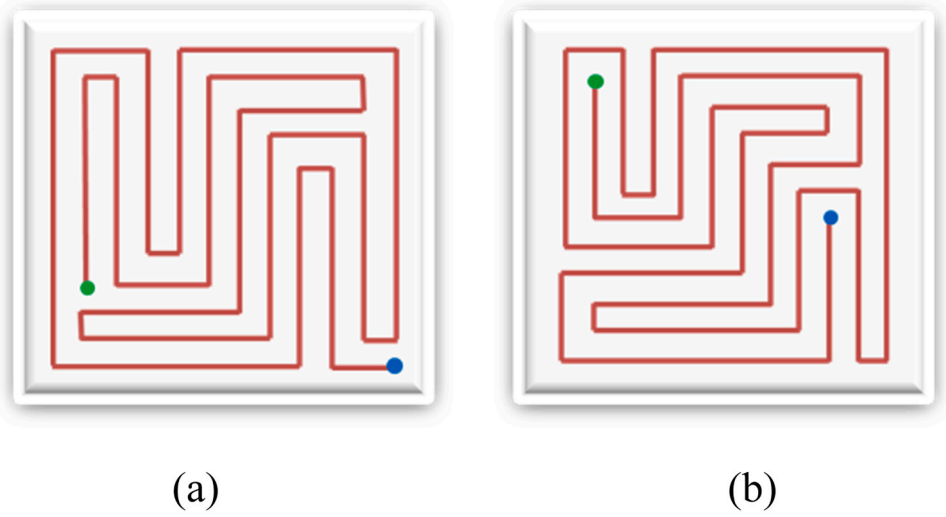

Fig. 14. New patterns proposed by the search algorithms. (a) S_1 (U=0.41); (b) S_2 (U=0.38). The green and blue dots are the starting and ending points, respectively. Both patterns have a similar shape to the S pattern and low U. The deposition sequence concentration is avoided by changing deposition directions. They are contour parallel patterns from inside to outside.

The mechanical properties of aluminum alloy AA2319 are displayed in Table 2. The temperature-dependent constitutive relationship of true stress and true strain is presented in Fig. 7.

3.2. The relationship between the residual stress and U

As a demonstration, we created a square deposition area which is divided into 144 square beads. Each bead has a size of 10 mm * 10 mm. All beads are numbered according to the bead sequence given by the different patterns. The $\overline{N}$ of each bead of different patterns are calculated based on Eqs. (1–3) and shown in Appendix Fig. A1. As shown in Fig. 8, drastically different distributions of $\overline{N}$ are observed for the patterns considered. It can be seen that the $\overline{N}$ distributions of the raster and Zigzag patterns (Fig. 8(a) and (b)) are similar to each other and the $\overline{N}$ increases from top to bottom. The $\overline{N}$ of the out-in spiral pattern is higher in the center than that in the edge, which is opposite to that of the in-out spiral pattern. For these four patterns, the $\overline{N}$ becomes higher with the increase of bead sequence number since the deposition directions are constant (from top to bottom, from inside to outside, and from outside to inside) and the successive passes are adjacent to each other. However, for the S pattern and alternate-line pattern, the deposition directions change or the deposition passes alternate, which makes the large and small bead sequence numbers more scattered over the deposition area, and the distributions of $\overline{N}$ are more uniform.

The transient temperature distributions at the end of the deposition process for all patterns considered are presented in Fig. 9. Since the bead sequence determines the degree of heat accumulation, the temperature distribution is correlated with the $\overline{N}$ distribution. It can be seen from Fig. 9 that the temperature distribution of the S pattern and alternate-line patterns are more uniform than those of other patterns, similar to the $\overline{N}$ distribution shown in Fig. 8. It is because the successive deposition vectors of the alternate-line and S patterns are both nonadjacent. Since

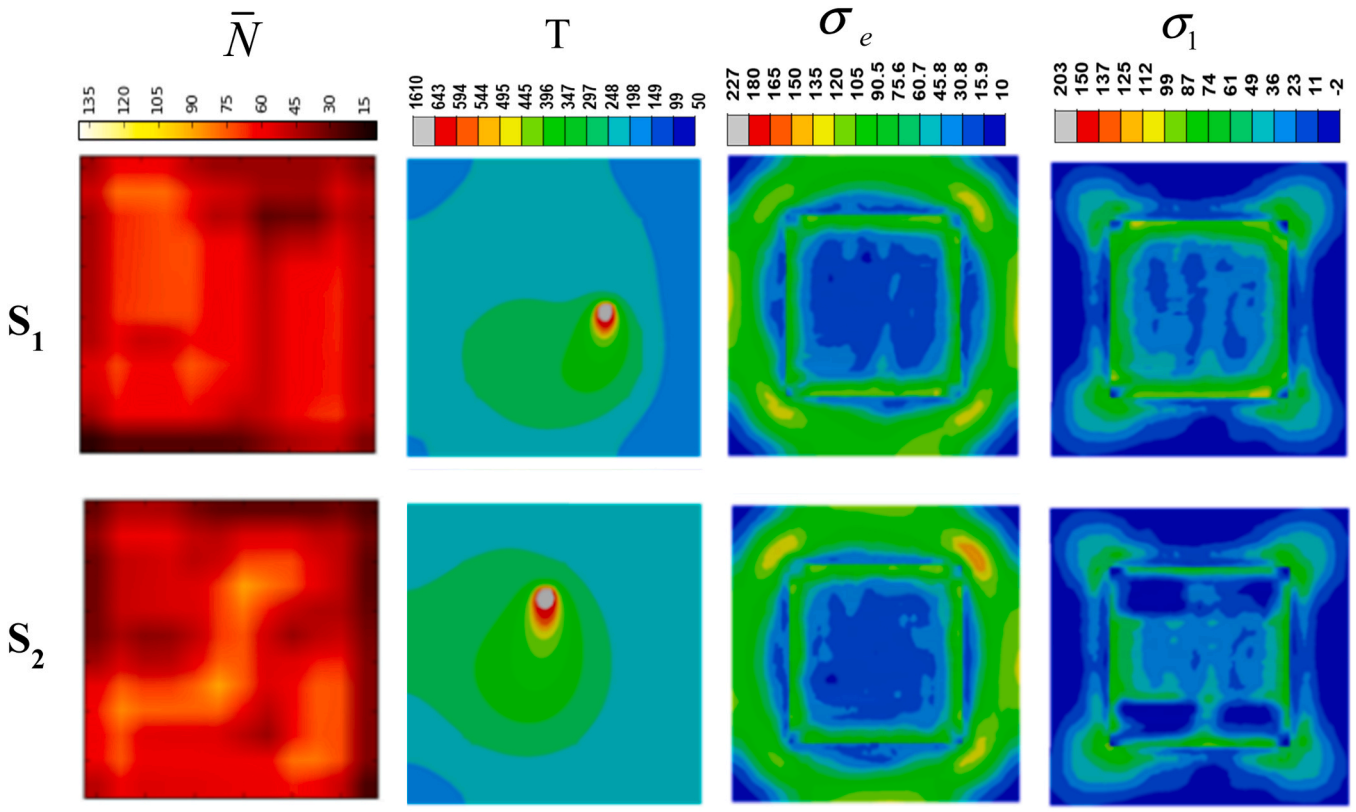

Fig. 15. The distributions of $\overline{N}$, temperature distribution, and residual stresses (σ_e and σ_1) distributions of two new patterns (S_1 and S_2).

the heat is accumulated inward, the out-in spiral deposition pattern has the most concentrated heat distribution, which is also consistent with the $\overline{N}$ distribution.

We also plot the equivalent residual stress (σ_e) and maximum principal residual stress (σ_1) fields in Fig. 10 and Fig. 11, respectively. Both the σ_e and σ_1 are very important parameters for detecting plastic deformation and fracture. Consistent with the results of the distribution of $\overline{N}$ and temperature, the alternate pattern and S pattern can generate more uniform residual stresses distribution, while the out-in pattern has the most inhomogeneous residual stresses distribution. As the residual stress distribution is determined by the temperature gradient, the homogeneity of residual stress distribution is positively correlated with the uniformity of temperature and $\overline{N}$ distributions, which are supported by Figs. 8–11.

Fig. 12 provides an overview of the deposition patterns and their corresponding $\overline{N}$ distributions, temperature distributions, and residual stress distributions. It can be observed that the distributions of the $\overline{N}$, temperature and residual stress become more uniform as the U decreases. It strengthens the conclusion that the uniformity of temperature and residual stress distributions is strongly correlated with the uniformity of $\overline{N}$ distribution. The U can be treated as the criterion to evaluate the deposition patterns.

In order to further explore the relationship between the residual stress and U, the highest residual stresses (σ_e and σ_1) of all patterns normalized by the yield stress (σ_Y) are plotted against the U in Fig. 13. Interestingly, both σ_e/σ_Y and σ_1/σ_Y follows a linear fit with the U:

$$\frac{\sigma_e}{\sigma_Y} = 0.081 + 1.030 * U \tag{8}$$

$$\frac{\sigma_1}{\sigma_Y} = 0.026 + 1.285 * U \tag{9}$$

The average errors of the normalized highest σ_e and σ_1 of all patterns are 4.6% and 1.5%, respectively. It becomes apparent that the U can serve as a criterion to evaluate the deposition pattern regarding residual stresses. Under the same deposition process parameters and with the same structure, the residual stress distributions become more uniform as U decreases, and the highest residual stresses linearly increase with the increase of U. Another finding is that among all the patterns, the S pattern has the lowest U (0.368) and simultaneously displays the lowest residual stress. Hence, the S pattern can be regarded as the optimum pattern for the square structure.

4. Application of the evaluation criterion - exploring new patterns to reduce residual stress

In addition to evaluating the existing patterns, the proposed criterion can also be used to search for new and improved patterns. In this work, a script for exploring new patterns for the demonstration model in Section 3 is developed and implemented in Matlab. New patterns should satisfy the following conditions: firstly, the sequential beads must be adjacent to each other, i.e., no spatial intermittent in the pattern; secondly, the whole target deposition area (144 grids) will be completely covered without any repetition for all the grids. Then, a conditional enumeration method is developed to find an optimized pattern. Here, we aim to find new patterns with lower U, and the target function is defined as:

$$U = \frac{\overline{N}_{\max} - \overline{N}_{\min}}{X} < 0.5 \tag{10}$$

In the script, a group of arrays was created to represent the location information of the 144 grids of the deposition region. Then the arrays are arranged and combined. The conditional enumeration method is applied. Finally, the patterns following the two aforementioned requirements and fulfilling the target functions will be automatically outputted from the script. Most of the output patterns are irregular with a large number of turns. The feedstock and heat input can be easily excessive at these turns, which will increase the deviations and lower the deposition efficiency. They are difficult to be extended to other structures. Among all the patterns resulted from the search algorithms, only two patterns have few turns, as shown in Fig. 14.

In order to further verify the proposed evaluation criterion, the $\overline{N}$ of these two new patterns are calculated by Eqs. (1–3) and thermal-mechanical FE simulations are performed to compute the temperature fields and residual stresses. The distributions of the $\overline{N}$, temperature and residual stress of the new patterns (see Fig. 15) are more uniform than those of other patterns (see Fig. 12) except for the S pattern. The normalized highest σ_e of the new patterns are 0.506 and 0.481, and the normalized highest σ_1 are 0.613 and 0.543, respectively. These results agree with the linear Eqs. (8) and (9) very well. The S pattern and the new patterns have shorter deposition vector length, fewer adjacent deposition segments, and outward deposition direction, which favors the reduction of residual stress as mentioned in Section 1. Furthermore, the new patterns possess many advantages i.e. continuous, few pattern elements, allowing to generate weave pattern, and alternate directions et.al. Both the S pattern and the two new patterns can be considered as the optimal patterns for the square structure.

5. Concluding remarks

This study proposes a bead sequence-driven method to evaluate and optimize the deposition patterns with the purpose of reducing residual stress. In this method, the deposition pattern is discretized into a series of beads represented by a sequence number. Based on the bead sequence number, we introduce two interconnected concepts: “equivalent bead sequence number” and “bead sequence number dispersion index” which can be physically interpreted as the representation of the localized heat accumulation and the global heat accumulation gradient, respectively. The proposed evaluation criterion is supported by the results of finite element simulation of a square part with six typical deposition patterns. According to the proposed criterion, two new patterns with lower residual stresses are obtained by a search algorithm. Following conclusions can be drawn:

1. The homogeneity of temperature and residual stresses distributions increases with the uniformity of the equivalent bead sequence number $\overline{N}$ distribution.
2. Both the highest equivalent residual stress and maximum principal residual stress of a pattern linearly increase with its corresponding value of bead sequence number dispersion index, U. The U can be easily calculated once the deposition sequence is known, and can be used as the criterion for evaluating and optimizing deposition patterns for the purpose of minimizing residual stress in additive manufacturing.
3. Among all the patterns, the S pattern with the lowest U yields the lowest equivalent residual stress and maximum principal residual stress and can be considered as the optimum pattern for printing square structures.

The proposed method is the first attempt to evaluate and optimize the deposition pattern with respect to residual stress based on the information readily available from the G-Code design. in additive manufacturing. For metal additive manufacturing, since any arbitrary geometry of a single layer can be represented by the bead sequence given by the scanning pattern, the proposed sequence-driven approach provides a new idea for real-time evaluation and optimization of the deposition pattern the proposed criterion and has the potential to be extended to different structures, materials, and additive manufacturing processes for path optimization. However, the HIZ size may slightly depend on the thermal transfer process which is associated with the complexity of the geometry, material, and deposition process. For a specific process that deviates significantly from the process considered in this study, the validity of the HIZ size must be carefully studied. Besides, in order to simplify the evaluation process, the effect of thermal boundary conditions on $\overline{N}$ value was ignored. For some complex structures, for example, with multiple irregular voids, the calculation method of $\overline{N}$ may need to be modified considering the actual heat transfer situation. The applicability of the proposed criterion will be possibly reduced with the increase of the complexity of printed structures. Future work should dedicate to verify the applicability of the proposed approach such that its capability and limitation can be clearly identified.

We have also identified the following topics for future research: (1) more studies should be undertaken to explore the optimum patterns for other structures i.e., thin-walled, cuboid, or more complex structures; (2) new deposition strategies can be developed by combining the proposed criterion with the intermittent strategy or island pattern. The optimal scan order of intermittent segments or islands can be explored using the proposed method by specifying the line length and the number of interrupts, or the size of the island. (3) in general, two kinds of deposition process parameters can significantly affect the heat transfer performance. One is in time scale, i.e., power, deposition speed, intermittent time, which determines the heat input. The other one is in spatial scale, i.e., the deposition pattern, which affects the degree of heat concentration. In this work, we focused on processes with continuous patterns, uniform energy power, and deposition speed. In the future, more variables can be introduced into this method to evaluate heat accumulation and reduce residual stress.

CRediT authorship contribution statement

Li Sun: Conceptualization, Methodology, Formal analysis, Software, Formal analysis, Writing – original draft, Writing – review & editing, Visualization. **Xiaobo Ren:** Supervision, Formal analysis, Writing – review & editing, Visualization, Funding acquisition. **Jianying He:** Resources, Writing – review & editing, Supervision. **Zhiliang Zhang:** Resources, Methodology, Formal analysis, Writing – review & editing, Supervision, Project administration, Funding acquisition.

Declaration of Competing Interest

The authors declare that they have no known competing financial interests or personal relationships that could have appeared to influence the work reported in this paper.

Acknowledgment

This research is funded by the China Scholarship Council (China) and the Research Council of Norway (Norway) through the Petromaks2 program (Project No. 281927) and the BIA Program (Project No. 269558).

Appendix

See Fig. A1 here.

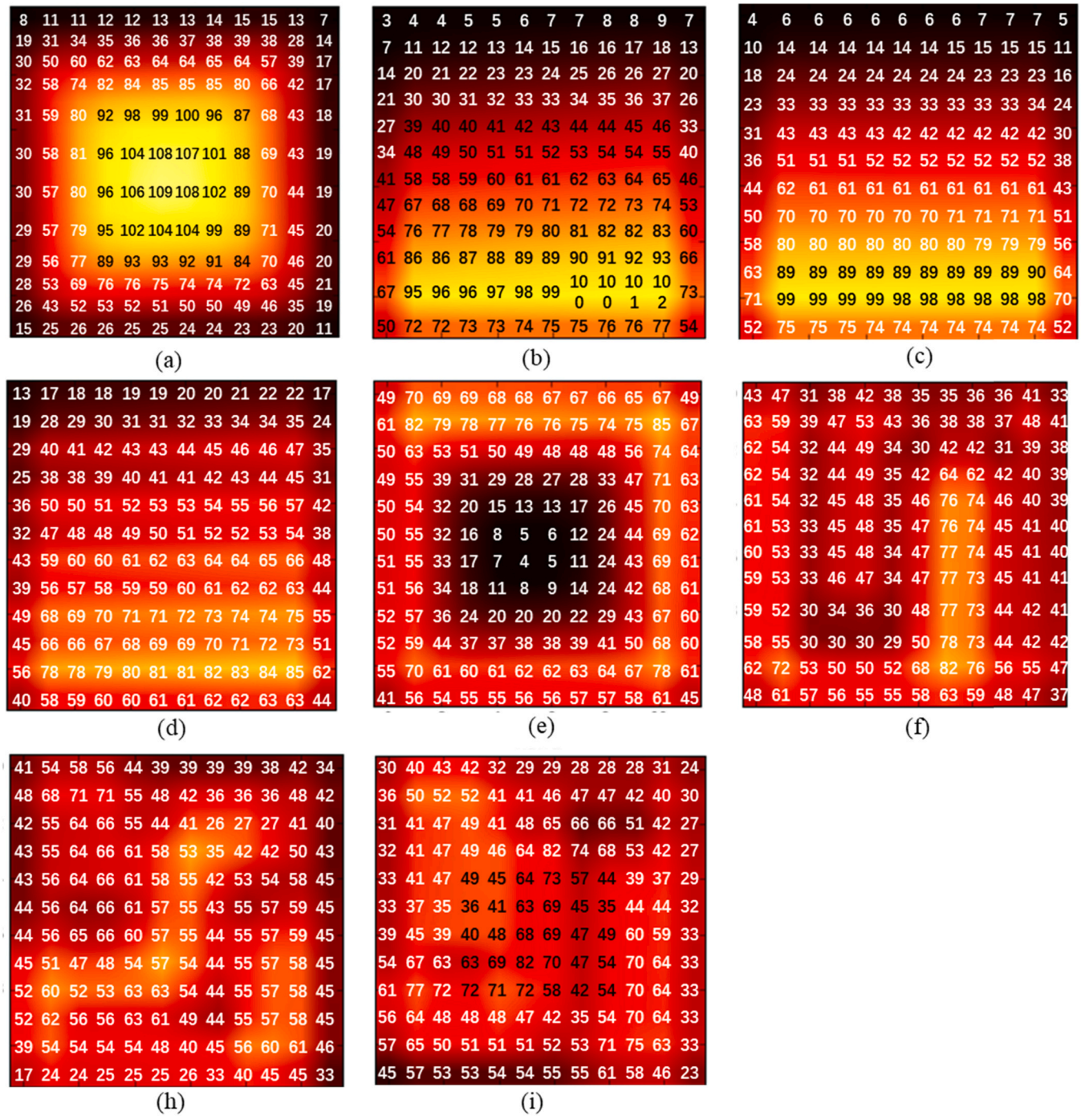

Fig. A1. The $\overline{N}$ distribution the corresponding contour graphs of the patterns studied in this work (a) Out-in spiral; (b) Raster; (c) Zigzag; (d) Alternate-line; (e) In-out spiral; (f) S; (h) S_1; (i) S_2.

References

[1] T. Pinomaa, I. Yashchuk, M. Lindroos, T. Andersson, N. Provatas, A. Laukkanen, Process-structure-properties-performance modeling for selective laser melting, Metals 9 (11) (2019) 1138.

[2] T. DebRoy, H.L. Wei, J.S. Zuback, T. Mukherjee, J.W. Elmer, J.O. Milewski, A. M. Beese, A. Wilson-Heid, A. De, W. Zhang, Additive manufacturing of metallic components – process, structure and properties, Prog. Mater. Sci. 92 (2018) 112–224.

[3] Y. Chew, J.H.L. Pang, G. Bi, B. Song, Thermo-mechanical model for simulating laser cladding induced residual stresses with single and multiple clad beads, J. Mater. Process. Technol. 224 (2015) 89–101.

[4] C.E. Seow, J. Zhang, H.E. Coules, G. Wu, C. Jones, J. Ding, S. Williams, Effect of crack-like defects on the fracture behaviour of Wire+ Arc additively Manufactured nickel-base Alloy 718, Addit. Manuf. 36 (2020), 101578.

[5] M. Roy, R. Yavari, C. Zhou, O. Wodo, P. Rao, Prediction and experimental validation of part thermal history in the fused filament fabrication additive manufacturing process, J. Manuf. Sci. Eng. 141 (12) (2019).

[6] M. Roy, O. Wodo, Quality assurance in additive manufacturing of thermoplastic parts: predicting consolidation degree based on thermal profile, Int. J. Rapid Manuf. 8 (4) (2019) 285–301.
[7] L. Sun, X. Ren, J. He, Z. Zhang, Numerical investigation of a novel pattern for reducing residual stress in metal additive manufacturing, J. Mater. Sci. Technol. 67 (2021) 11–22.
[8] S. Routhu, D. Kanakanala, J. Ruan, X.F. Liu, F. Liou, 2-D path planning for direct laser deposition process, ASME 2010 International Design Engineering Technical Conferences and Computers and Information in Engineering Conference, Am. Soc. Mech. Eng. Digit. Collect. (2010) 415–423.
[9] A. Schröffer, J. Prsa, F. Irlinger, T.C. Lüth, A novel building strategy to reduce warpage in droplet-based additive manufacturing of semi-crystalline polymers, 2018 IEEE International Conference on Robotics and Biomimetics (ROBIO), IEEE (2018) 1894–1899.
[10] W. Zhang, M. Tong, N.M. Harrison, Scanning strategies effect on temperature, residual stress and deformation by multi-laser beam powder bed fusion manufacturing, Addit. Manuf. 36 (2020), 101507.
[11] D. Ramos, F. Belblidia, J. Sienz, New scanning strategy to reduce warpage in additive manufacturing, Addit. Manuf. 28 (2019) 554–564.
[12] A.S. Wu, D.W. Brown, M. Kumar, G.F. Gallegos, W.E. King, An experimental investigation into additive manufacturing-induced residual stresses in 316L stainless steel, Metall. Mater. Trans. A 45 (13) (2014) 6260–6270.
[13] Y. Lu, S. Wu, Y. Gan, T. Huang, C. Yang, L. Junjie, J. Lin, Study on the microstructure, mechanical property and residual stress of SLM Inconel-718 alloy manufactured by differing island scanning strategy, Opt. Laser Technol. 75 (2015) 197–206.
[14] J.-P. Kruth, J. Deckers, E. Yasa, R. Wauthlé, Assessing and comparing influencing factors of residual stresses in selective laser melting using a novel analysis method, Proceedings of the institution of mechanical engineers, Part B J. Eng. Manuf. 226 (6) (2012) 980–991.
[15] M. Somashekara, M. Naveenkumar, A. Kumar, C. Viswanath, S. Simhambhatla, Investigations into effect of weld-deposition pattern on residual stress evolution for metallic additive manufacturing, Int. J. Adv. Manuf. Technol. 90 (5–8) (2017) 2009–2025.
[16] N. Nazemi, R.J. Urbanic, A numerical investigation for alternative toolpath deposition solutions for surface cladding of stainless steel P420 powder on AISI 1018 steel substrate, Int. J. Adv. Manuf. Technol. 96 (9–12) (2018) 4123–4143.
[17] W. Yan, Z. Yue, J. Feng, Study on the role of deposition path in electron beam freeform fabrication process, Rapid Prototyp. J. 23 (2017) 1057–1068.
[18] J.L. Bartlett, X. Li, An overview of residual stresses in metal powder bed fusion, Addit. Manuf. 27 (2019) 131–149.
[19] J.-P. Kruth, M. Badrossamay, E. Yasa, J. Deckers, L. Thijs, J. Van Humbeeck, Part and material properties in selective laser melting of metals, Proceedings of the 16th international symposium on electromachining, 2010, pp. 1–12.
[20] L. Parry, I. Ashcroft, R.D. Wildman, Understanding the effect of laser scan strategy on residual stress in selective laser melting through thermo-mechanical simulation, Addit. Manuf. 12 (2016) 1–15.
[21] L. Parry, I. Ashcroft, R. Wildman, Geometrical effects on residual stress in selective laser melting, Addit. Manuf. 25 (2019) 166–175.
[22] M.F. Zaeh, G. Branner, Investigations on residual stresses and deformations in selective laser melting, Prod. Eng. 4 (1) (2010) 35–45.
[23] B. Cheng, S. Shrestha, K. Chou, Stress and deformation evaluations of scanning strategy effect in selective laser melting, Addit. Manuf. 12 (2016) 240–251.
[24] M. Köhler, L. Sun, J. Hensel, S. Pallaspuro, J. Kömi, K. Dilger, Z. Zhang, Comparative study of deposition patterns for DED-Arc additive manufacturing of Al-4046, Mater. Des. 210 (2021), 110122.
[25] J.L. Bartlett, B.P. Croom, J. Burdick, D. Henkel, X. Li, Revealing mechanisms of residual stress development in additive manufacturing via digital image correlation, Addit. Manuf. 22 (2018) 1–12.
[26] A.J. Wolfer, J. Aires, K. Wheeler, J.-P. Delplanque, A. Rubenchik, A. Anderson, S. Khairallah, Fast solution strategy for transient heat conduction for arbitrary scan paths in additive manufacturing, Addit. Manuf. 30 (2019), 100898.
[27] K. Ren, Y. Chew, Y. Zhang, J. Fuh, G. Bi, Thermal field prediction for laser scanning paths in laser aided additive manufacturing by physics-based machine learning, Comput. Methods Appl. Mech. Eng. 362 (2020), 112734.
[28] A. Paul, M. Mozaffar, Z. Yang, W.-k Liao, A. Choudhary, J. Cao, A. Agrawal, A real-time iterative machine learning approach for temperature profile prediction in additive manufacturing processes, arXiv Prepr. arXiv 1907 (2019), 12953-550.
[29] M. Roy, O. Wodo, Data-driven modeling of thermal history in additive manufacturing, Addit. Manuf. 32 (2020), 101017.
[30] Y. Javadi, C.N. MacLeod, S.G. Pierce, A. Gachagan, D. Lines, C. Mineo, J. Ding, S. Williams, M. Vasilev, E. Mohseni, Ultrasonic phased array inspection of a Wire+ Arc Additive Manufactured (WAAM) sample with intentionally embedded defects, Addit. Manuf. 29 (2019), 100806.
[31] C. Wang, W. Suder, J. Ding, S. Williams, The effect of wire size on high deposition rate wire and plasma arc additive manufacture of Ti-6Al-4V, J. Mater. Process. Technol. 288 (2020), 116842.
[32] T. Pinomaa, M. Lindroos, M. Walbrühl, N. Provatas, A. Laukkanen, The significance of spatial length scales and solute segregation in strengthening rapid solidification microstructures of 316L stainless steel, Acta Mater. 184 (2020) 1–16.
[33] K. Ren, Y. Chew, J.Y.H. Fuh, Y.F. Zhang, G.J. Bi, Thermo-mechanical analyses for optimized path planning in laser aided additive manufacturing processes, Mater. Des. 162 (2019) 80–93.
[34] K. Ren, Y. Chew, Y.F. Zhang, G.J. Bi, J.Y.H. Fuh, Thermal analyses for optimal scanning pattern evaluation in laser aided additive manufacturing, J. Mater. Process. Technol. 271 (2019) 178–188.
[35] L. Sun, X. Ren, J. He, J.S. Olsen, S. Pallaspuro, Z. Zhang, A new method to estimate the residual stresses in additive manufacturing characterized by point heat source, Int. J. Adv. Manuf. Technol. 105 (5–6) (2019) 2415–2429.
[36] J. Ding, Thermo-mechanical Analysis of Wire and Arc Additive Manufacturing Process, Cranfield University, United Kingdom, 2012.
[37] P. Ferro, F. Berto, N.M. James, Asymptotic residual stress distribution induced by multipass welding processes, Int. J. Fatigue 101 (2017) 421–429.
[38] P. Michaleris, Feng, Z., and Campbell, G., Evaluation of 2D and 3D FEA Models for Predicting Residual Stress and Distortion, ASME PVP- Approximate Methods in the Design and Analysis of Pressure Vessels and Piping Components 347 (1997) 91–102.
[39] U Y. Yuan MG , Prediction of Residual Stresses in Welded T- and l-Joints Using Inherent Strains, Journal of Engineering Materials and Technology 118((2)) (Yuan MG, Ueda Y.) 229–234.
[40] Abaqus Analysis User's Guide , Abaqus 2018, Dassault Systèmes Simulia Corp., 2018.